A Review of the State Space Method for Model-Based Extraction of Electromagnetic Parameters in Radar and Scattering Problems

Krishna Naishadham [(1)] and Jean E. Piou [(2)]
[(1)] Georgia Institute of Technology, Atlanta, GA, USA
Email: krishna.n@ieee.org
[(2)] Private Researcher, Lexington, MA, USA
Email: jepiou@gmail.com

***Abstract* — As computing power and algorithmic advances have evolved significantly in the recent past, it is now feasible to solve complex electromagnetic (EM) problems involving scattering, radar cross section, antenna design, microwave circuit design, artificial EM materials, etc. using full-wave numerical methods. Several general-purpose commercial software packages are routinely used in industry in all these domains for EM analysis or design. However, the task of processing large sets of data output from these design studies and analyses is generally beyond the realm of commercial software packages, and the designer spends many hours writing problem-specific computer programs to extract the desired performance parameters. Determination of coupling coefficients or the unloaded quality factor of a dielectric resonator, de-embedding feed lines from antenna currents, removal of discontinuity effects, the extraction of equivalent circuit models, etc. are some examples where auxiliary processing is needed for the extraction of EM parameters of interest. The same considerations apply to the parametric analysis of measured data in the presence of noise. This paper presents a versatile data-driven spectral model derived from a *state-space system representation* of the computed or measured EM fields, from which all the parameters of interest can be extracted. Several examples will be presented to demonstrate the usefulness of the proposed approach for parametric extraction in EM problems.**

***Index Terms* —Electromagnetic Scattering, Finite Difference Time Domain, Finite Integration Time Domain, Microwave Circuit, Microwave Resonator, Signal Extrapolation, Spectral Estimation, State Space Method, System Identification, Transient Analysis, Transmission Line**

I. INTRODUCTION

With prolific algorithmic advances and significant improvement of computational resources in recent years, full-wave electromagnetic (EM) simulation techniques, such as the method of moments (MoM) [1], the finite element method (FEM) [2], the finite-difference time-domain (FDTD) method [3] and the transmission line matrix method [4], are increasingly used to solve complex EM problems involving scattering, radar cross section (RCS), antenna design, microwave circuit design, artificial EM materials, etc. These rigorous techniques account for physical phenomena such as surface-wave coupling and radiation, dispersion, frequency-dependent metallization and dielectric losses, proximity effects and near-field coupling. Although EM simulation methods are computationally intensive in practice, large-scale GPU and distributed computing enables commercially available full-wave EM analysis software packages to be applied to challenging problems such as scattering by electrically large objects (e.g., computing the RCS of an aircraft) and modeling the EMI between interconnects on a printed circuit board containing dense RF and/or high-speed digital circuits. The outputs of these software packages are generally voltages, currents, scattering (S) parameters or some derived EM field variable such as the RCS. In design studies large datasets of these output parameters need to be processed, for example, to remove the effects of transmission line discontinuities on the S-parameters or to extract the modal response of a particular wave species and isolate the scattering centers causing undesirable RCS. Therefore, it is very desirable to investigate independent signal models (in time domain) and spectral models (in frequency domain), which accurately represent the simulated or measured output fields. One can then utilize this model for removing the effects of discontinuities or parasitic scattering mechanisms so that the desired EM performance can be characterized accurately.

Several researchers have extracted parameters of interest from scattered fields or circuit response using signal processing techniques such as Prony's method [5], [6], pencil of functions [7]-[11], autoregressive moving average (ARMA) [12], [13], estimation of signal parameters via rotational invariance techniques (ESPRIT) [14]-[16], multiple signal classification (MUSIC) [17], and the state space method (SSM) [18]-[21]. Applications include computation of complex natural resonances and eigenmodes [22]-[28], impulse response characterization of time-domain signatures [29]-[34], broadband circuit parameter extraction [35], [36], identification of radar target's features [37]-[40], extraction of

biomedical vital signs from UWB radar measurements [41]-[43], and location of buried targets using ground penetrating radar [44]. The basis behind such signal processing application is that the EM field scattered by an object can be adequately represented as a sum of damped sinusoids, whose amplitude and phase are closely related to the physical parameters of interest. For example, poles of the transfer function for the exponential signal model locate discrete scattering centers useful in object typing and feature identification in radar target identification.

This paper presents a versatile data-driven spectral model derived from a state-space system representation of the *computed* or *measured* scattering parameters and EM fields, from which all the parameters of interest can be extracted. Parametric extraction from measured data is especially challenging because of noise and random measurement errors. The efficacy of spectral estimation methods to extract parameters of damped sinusoids embedded in noise has been studied by many researchers. For example, performance analysis of MUSIC is treated in [45], [46], estimation of the direction of arrival of radar returns using ESPRIT is presented in [47], a performance study of matrix pencil method in the presence of noise is described in [48], [49], and sensitivity analysis of the state space method is treated in [50], [51]. SSM [18]-[21] has been extended to ultra-wideband coherent processing of range-Doppler data for radar target identification and validated with static range measurements [52]-[54]. A comparative analysis between state space and matrix pencil methods shows similar performance with comparable accuracy when implemented on harmonic retrieval problems with noisy data [49], [55], [56].

The reader is referred to [40]-[43], [52]-[54] for the application of SSM to feature identification using monostatic RCS *measured data* on stationary targets as well as human subjects. As we have shown in [40] using measured data on a large conical target with and without a lossy dielectric coating, the isolation of electromagnetic wave species of interest, such as creeping waves, multiply diffracted waves and specular scattering, yields a better understanding of the physics behind wave propagation around curved dielectric or coated structures, thereby improving the accuracy of feature extraction or target identification. For example, it has been shown that the coating enhances the creeping wave contribution significantly in certain directions compared to the metallic cone, suggesting its efficacy in absorbing EM waves [40]. The biomedical UWB radar [41]-[43] uses narrow pulses to probe the human body and detect tiny cardiopulmonary movements by spectral analysis of the backscattered EM field. With the help of super-resolution spectral algorithms [52]-[54], UWB radar is capable of increased accuracy for estimating vital signs such as heart and respiration rates in adverse signal-to-noise conditions. A major challenge for biomedical radar systems is detecting the heartbeat of a subject with high accuracy, because of minute thorax motion (less than 0.5 mm) caused by heartbeat. The problem becomes compounded by EM clutter and noise in the environment. We have shown that SSM processing of the UWB radar data on a stationary human subject consistently produces accurate estimates of the vital signs for several channels of UWB data without producing harmonics and inter-modulation products that plague signal resolution in widely used FFT spectrograms [41].

The state space method can be applied in either time domain or frequency domain. In this paper, we focus on the frequency domain problems. The reader is referred to [34] for the application of SSM to time-domain EM problems. An attractive feature of SSM is its ability to identify and associate a small number of poles of the system transfer function with a specific scattering mechanism or modal response, such as scattering parameters at the transition between a coaxial connector and a microstrip transmission line in measured data, and isolated scattering by edges and seams from the composite RCS of a large body. Thus, the desired field parameter can be extracted or estimated from synthetic or measured data using a linear system with relatively small model order. Illustrative examples will be presented to demonstrate the usefulness of the state space method for parametric extraction in EM problems. We describe the problem formulation and the modeling process in detail so that an uninitiated reader can follow the steps to program and execute the algorithm and generate results of interest.

In the first example, we consider a planar dielectric slab illuminated by a plane wave at normal incidence and isolate the reflection off the front face using range-classified poles pertinent to the specular reflection. This process is akin to de-embedding transmission lines at the ports to evaluate the circuit behavior of an antenna or a discontinuity. In the second example, appealing to the canonical problem of Mie scattering by a sphere, creeping waves are extracted using SSM to model the RCS response, and validated against high-frequency asymptotic approximations. Next, random white Gaussian noise is added to the Mie series solution, and Monte Carlo simulation is performed to examine robustness of the SSM estimates to noise. Numerical considerations such as dynamic range, signal-to-noise ratio (SNR) and model order determination are addressed in detail for both examples.

The paper is organized as follows. In Section II the state space algorithm is reviewed in detail following [52], [53]. Section III presents basic numerical considerations on the state space approach, such as estimating the SNR and the model order. Section IV presents illustrative examples on parametric extraction for EM problems, as discussed earlier. Factors affecting accuracy and numerical efficiency of the proposed technique are discussed. Finally, some concluding remarks are provided in Section V.

II. State Space Method

In recent years, there has been a great deal of attention devoted to model-based eigen-decomposition methods derived from a state-space realization of the system identification problem, which is defined as the determination of the internal states of a linear time-invariant (LTI) system given a set of inputs and outputs [18], [21], [52]-[62]. The idea of using state-space methods to estimate frequencies and amplitudes of damped sinusoids was first suggested in [18], where Kung et al. developed a system identification approach based on singular value decomposition (SVD) for the

harmonic retrieval (or spectral estimation) problem. The foundation of state-space signal modeling is based on representation of a linear rational system, popular in linear systems and control theory [63]-[65], in which the difference equations for the discrete-time (or discrete-frequency) signal are converted into state equations and the model parameters are estimated in terms of the state matrices characterizing the system. State-space parameterization enables reduction of parameter sensitivity, as demonstrated by several examples relevant to the sinusoid retrieval problem in the tutorial article by Rao and Arun [21]. Unlike polynomial-based signal processing methods such as Prony's, MUSIC and maximum likelihood estimation, in which the frequencies are obtained by cumbersome root-search of the polynomials, state-space methods simultaneously yield complex amplitudes (with initial phases) and frequencies directly from three *state matrices*. The frequencies are calculated from the eigenvalues of the *state transition matrix*, and the amplitudes are derived by modal eigen-decomposition of the state equations using two auxiliary matrices, the *control and observation matrices*.

As shown in the sequel, because the decomposition of the data into a sum of damped sinusoids gives rise to an LTI system, the state matrices can be readily computed via a low-rank truncation of the *Hankel* (or *forward-prediction*) matrix representing the data. Thus, each entry of the Hankel matrix can be expressed in terms of the impulse response derived from the state space matrices. The SVD of the Hankel matrix is a product of the *observability* and *controllability* matrices which yield all the model parameters in the harmonic retrieval using state dimensions corresponding to the number of scatterers embedded in the data.

A. ARMA Signal Model

The scattered field output data sequence $y(k)$ comprises N uniformly spaced frequency samples (see (1) below), each represented as a sum of M complex sinusoids (or scattering centers) corrupted by measurement noise $w(k)$, assumed to be white Gaussian with zero mean. In deterministic data modeling we assume that $w(k)=0$ and characterize the impulse response, thus estimating the system parameters using only the output. When the input is known and needs to be considered (e.g., short pulses or modulated waveforms) the system can be identified using both input $w(k)$ and output $y(k)$ [34]. For completeness we retain $w(k)$ in the formulation even if we may not consider it in a given case. Thus, over a given bandwidth, the signal measurements at N frequencies are modeled as

$$y(k)=\sum_{i=1}^{M} a_i e^{(\alpha_i + j2\pi\tau_i) f_k} + w(k); \quad k=1,\cdots,N, \qquad y(k)=\hat{y}(k)+w(k). \tag{1}$$

The difference between the "true" signal (or truth), $y(k)$, and the state space model, $\hat{y}(k)$, is the random noise, measurement or modeling error, $w(k)$. The model parameters a_i and α_i represent the amplitude and its spectral rate of decay (for negative α_i) or growth (for positive α_i), respectively, for the i-th scattering center. Both positive and negative α_i are needed to model the peaks and dips in the frequency response (for example at resonance). It is emphasized that positive α_i does not imply instability or violation of any physical constraint such as the radiation condition. The parameter τ_i denotes time delay of the i-th scatterer at the observation point and is related to range R_i by $\tau_i = 2R_i/c$, where c is the speed of light. Equation (1) is set up in terms of the monostatic RCS that an observer would measure for a given target at range R_i. Therefore, $2R_i$ is simply the round-trip distance between the transmitter and the target. If bistatic radar is used, then $2R_i$ should be replaced by $R_t + R_r$, where R_t and R_r denote the distance to the target from the transmitter and the receiver, respectively. It follows that $2\pi\tau_i f_k = (\omega_k/c)(2R_i) = \beta_k(2R_i)$ represents the phase of the i-th sinusoid, with β_k being the phase constant at the frequency f_k. The frequency vector is specified in terms of the carrier frequency f_1 as

$$f_k = f_1 + (k-1)\Delta f, \quad k=1,\cdots,N, \tag{2}$$

where Δf is the sampling frequency. The primary interest in state space system identification is to estimate the parameters a_i, α_i and R_i (or τ_i), which are embedded in the data sequence $y(k)$. The latter two parameters are computed from the eigenvalues of an open-loop state matrix, to be defined shortly. Once these parameters are estimated, the amplitudes a_i can be readily derived from the state matrices using a modal decomposition method based on least squares [53].

B. ARMA Transfer Function

The ARMA model in (1) is interpreted as an LTI system with input given by the sequence $w(k)$ and the output by the data sequence $y(k)$. The goal in system identification is to compute the coefficients of the ARMA transfer function (TF) characterizing the discrete-frequency signal model in (1). Taking the z-transform of (1) after substituting f_k from (2), we obtain

$$Y(z)=\sum_{i=1}^{M}\frac{B_i}{1-p_i z^{-1}} + W(z) \tag{3}$$

$$B_i = a_i e^{\alpha_i f_1} \overbrace{e^{j2\pi\tau_i f_1}}^{\theta_i} \triangleq A_i e^{j\theta_i} \tag{4}$$

$$p_i = \alpha_i + j2\pi\tau_i \tag{5}$$

In (3) - (5) B_i denote the complex amplitudes, θ_i is the initial (static) phase, and p_i are the poles in the complex z-plane. The summation in (3) results in a TF comprising rational polynomials in the numerator and denominator:

$$T(z)=\frac{Y(z)}{W(z)}=\frac{c_0+\sum_{i=1}^{M-1} c_i z^{-i}}{1-\sum_{i=1}^{M} d_i z^{-i}} \triangleq \frac{N(z)}{D(z)} \tag{6}$$

The TF $T(z)$ has M poles and $M-1$ zeros, located at the roots of $D(z)$ and $N(z)$, respectively. The TF in (6) represents a special case of a more general ARMA TF given by

$$T(z)=\frac{c_0+\sum_{i=1}^{Q}c_i z^{-i}}{1-\sum_{i=1}^{P}d_i z^{-i}}\triangleq\frac{N(z)}{D(z)} \tag{7}$$

which has *P* poles and *Q* zeros (*P* and *Q* can assume arbitrary integer values). The special case $Q=P-1$ listed in (6) is also known as "strictly proper" TF and the Prony's model belongs to this category. Another important special case is the purely Auto Regressive (AR) TF with $Q=0$.

The input-output relationship for the general ARMA model with the TF in (7) is characterized by the difference equation

$$y(k)=\sum_{i=1}^{P}d_i y(k-i)+\sum_{j=1}^{Q}c_j w(k-j)+c_0 w(k) \tag{8}$$

Eq. (8) is valid for the TF in (6) as well with $P=M$ and $Q=(M-1)$. From linear systems and control theory [63], [64] one can show that the difference equation in (8) may be written alternatively in terms of the state-space description characterized by the difference equations

$$x(k+1)=Ax(k)+Bw(k) \tag{9}$$

$$y(k)=Cx(k)+w(k), \tag{10}$$

where $x(k)\in\mathbf{C}^{M\times 1}$ is the state, $A\in\mathbf{C}^{M\times M}$ is the *state transition matrix*, $B\in\mathbf{C}^{M\times 1}$ and $C\in\mathbf{C}^{1\times M}$ are constant matrices known as *control matrix* and *observation matrix*, respectively [64]. Our goal is to identify the matrices *A*, *B* and *C* given the data sequence *y*(*k*) and the input *w*(*k*). The transfer function, *T(z)*, is obtained by taking the *z*-transform of (9) and (10) and evaluating the ratio $Y(z)/W(z)$:

$$T(z)=C(zI-A)^{-1}B+1. \tag{11}$$

It follows from (11) that the poles of the model (i.e., the roots of *D*(*z*) in (7)) are the eigenvalues of the open-loop matrix *A* and the zeros (i.e., the roots of *N*(*z*) in (7)) are the eigenvalues of the matrix $(A-BC)$ [52], [53].

C. State Space System Identification

The transfer function in (7) can be written equivalently in terms of its impulse response sequence as

$$T(z)=h(0)+h(1)z^{-1}+\cdots+h(n)z^{-n}+\cdots \tag{12}$$

which is aptly referred to as the *infinite impulse response* (IIR) transfer function. The expansion of the inverse matrix in (11) into an infinite series yields

$$(zI-A)^{-1}=Iz^{-1}+Az^{-2}+A^2z^{-3}+\cdots \tag{13}$$

By inserting (13) into (11) we obtain

$$T(z)=1+CBz^{-1}+CABz^{-2}+CA^2Bz^{-3}+\cdots \tag{14}$$

Equating coefficients of like-powers of *z* in (12) and (14) and realizing that $h(k)=y(k)$ for the impulse input, we obtain

$$\begin{aligned} y(0)&=1\\ y(1)&=CB\\ y(2)&=CAB\\ &\vdots\\ y(k)&=CA^{k-1}B\\ &\vdots \end{aligned} \tag{15}$$

Therefore, the relationship between the impulse response of the model and the state-space parameters for any positive value of *k* is defined by

$$y(k)=CA^{k-1}B,\ k>0. \tag{16}$$

Eq. (16) indicates that a Hankel (or forward-prediction) matrix, *H*, formed from the IIR sequence of a system as

$$H=\begin{bmatrix} y(1) & y(2) & y(3) & \cdots\\ y(2) & y(3) & y(4) & \cdots\\ y(3) & y(4) & y(5) & \cdots\\ \vdots & \vdots & \vdots & \vdots \end{bmatrix} \tag{17}$$

can be decomposed into a product of two matrices given by

$$H=\begin{bmatrix} C\\ CA\\ CA^2\\ \vdots \end{bmatrix}\begin{bmatrix} B & AB & A^2B & \cdots \end{bmatrix}\triangleq\Omega\Gamma, \tag{18}$$

where Ω and Γ are known as *observability* and *controllability* matrices, respectively [65]. It is important to note that despite the infinite dimensions of *H* in (17), in practice the impulse response is always finite. Thus, for a given set of measurements the rank of the Hankel matrix *H*, and by inference the rank of Ω and Γ, will always be finite. As described later in this Section, Ω and Γ, consequently *H*, can be truncated to *low-rank matrices* with rank $r\le M$, where *M* is the number of complex sinusoids in the model (see (1)). In summary, the Hankel matrix *H* may be interpreted as an operator constructed from a set of measurements *y*(*k*) that maps the past input vector w^- to the future output y^+. *Causality of SSM is explicit in* (8) - (10)*, which emphasize that the current output is dependent on the past output and the current as well as the past input signals.* Next, we present a method to derive the state-space matrices from the Hankel matrix constructed using a finite set of output data samples.

The first step in computing the triplet (*A*, *B*, *C*) is to form the Hankel matrix using the available data samples $y(k),\ k=1,2,\cdots N.$

$$H=\begin{bmatrix} y(1) & y(2) & \cdots & y(L)\\ y(2) & y(3) & \cdots & y(L+1)\\ \vdots & \vdots & \vdots & \vdots\\ y(N-L+1) & y(N-L+2) & \cdots & y(N) \end{bmatrix} \tag{19}$$

where the parameter *L* denotes length of the correlation window, heuristically chosen to be $L=[N/2]$, and the brackets denote the smallest integer less than or equal to the inserted quantity. Note that the Hankel matrix in (19) is a truncated version of the IIR in (17). Subspace decomposition

methods exploit the eigenstructure of Hankel matrices to compute the state matrices of the LTI system and estimate the signal models [18], [21], [25], [26], [52]-[56], [60]-[62]. Accordingly, we partition the Hankel matrix into signal and noise subspaces using the singular value decomposition of *H*. Organizing the SVD in terms of the singular values $\{\sigma_i\}$ in descending order of magnitude, the Hankel matrix may be written as

$$H = \begin{bmatrix} U_s & U_n \end{bmatrix} \begin{bmatrix} \Sigma_s & 0 \\ 0 & \Sigma_n \end{bmatrix} \begin{bmatrix} V_s^* \\ V_n^* \end{bmatrix} = U \Sigma V^* \tag{20}$$

where the subscripts *s* and *n* denote the signal and noise subspaces, respectively, and the asterisk refers to matrix conjugate transpose. The matrices U_s and U_n are the signal and noise components, respectively, of the left-unitary matrix $[U_s \;\; U_n]$. Likewise, V_s and V_n denote the signal and noise components, respectively, of the right-unitary matrix $[V_s \;\; V_n]$. Furthermore, Σ_s and Σ_n are diagonal matrices comprising the signal and noise singular values, respectively. It is understood that the signal components in the SVD are entirely characterized by the dominant singular values Σ_s. The classification between signal and noise subspaces is achieved by parsing the singular value spectrum in descending order of magnitude and removing the noise singular values Σ_n [18], [50]-[53]. To increase the accuracy of the state-space matrices, the Hankel matrix *H* may then be truncated by suppressing the noise singular values and their associated unitary matrix components. This results in a reduced-rank approximation to the Hankel matrix in (20), obtained by retaining only the dominant singular values (cf. [51]), i.e.,

$$\tilde{H} = U_s \Sigma_s V_s^*. \tag{21}$$

Let the computed singular values in Σ be arranged in descending order of magnitude

$$\sigma_1 > \sigma_2 > \;\cdots\; > \sigma_r > 0 \tag{22}$$

where *r* is chosen subject to the threshold [53] $\sigma_r / \sigma_1 \approx 10^{-p}$, and p is the number of significant decimal digits in the truth data. For example, if the data is accurate to three significant digits, then the singular values with upper bound *r* for which the ratio is less than 0.001 are considered as noise singular values and excluded from the model. *The largest index r of the singular values in the signal subspace is the rank of the Hankel matrix*. It can be shown that the largest retained singular value minimizes the error between the Hankel matrices *H* and $\tilde{H}$ in the spectral norm sense [49], i.e.,

$$\sigma_r \approx \left\| H - \tilde{H} \right\|_s, \tag{23}$$

where the subscript *s* denotes the spectral or L_2 norm [64]. As demonstrated in Section III, magnitude of the dominant singular values in the signal subspace may be conveniently used to estimate the "optimal" model order *M* in (1). Next, we address how one can compute the state matrices from the SVD.

Akin to (18) $\tilde{H}$ is obtained in factored form as

$$\tilde{H} = U_s \Sigma_s V_s^* = \tilde{\Omega} \tilde{\Gamma} \tag{24}$$

By using the balanced coordinate transformation method proposed in [18], one can compute the *finite-rank observability matrix* $\tilde{\Omega}$ and *controllability* matrix $\tilde{\Gamma}$ from the SVD in (24). These matrices are given by

$$\tilde{\Omega} = U_s \Sigma_s^{1/2} \;\text{ and }\; \tilde{\Gamma} = \Sigma_s^{1/2} V_s^*. \tag{25}$$

Then, the open-loop matrix $A \in \mathbf{C}^{M \times M}$ can be derived from either $\tilde{\Omega}$ or $\tilde{\Gamma}$ as shown in the Appendix. If the derivation of *A* is based on the observability matrix $\tilde{\Omega}$, then [40]

$$A = \left(\tilde{\Omega}_{-r\ell}^* \tilde{\Omega}_{-r\ell} \right)^{-1} \tilde{\Omega}_{-r\ell}^* \tilde{\Omega}_{-r1}. \tag{26}$$

The matrices $\tilde{\Omega}_{-r1}$ and $\tilde{\Omega}_{-r\ell}$ in (26) are obtained by deleting the first and last rows, respectively, of $\tilde{\Omega}$. Alternatively, in terms of the controllability matrix, *A* is given by [40]

$$A = \tilde{\Gamma}_{-c1} \tilde{\Gamma}_{-c\ell}^* (\tilde{\Gamma}_{-c\ell} \tilde{\Gamma}_{-c\ell}^*)^{-1} \tag{27}$$

where the matrices $\tilde{\Gamma}_{-r1}$ and $\tilde{\Gamma}_{-r\ell}$ are obtained by deleting the first and last rows, respectively, of $\tilde{\Gamma}$. The reader is referred to the Appendix for the least-squares computation of *B* and *C*, also using either $\tilde{\Omega}$ or $\tilde{\Gamma}$. As noted earlier, the matrices *B* and *C* contribute to zeros of the transfer function. In the AR SSM that we have employed in [39], these two matrices are not used, because the system is entirely characterized by the poles determined from *A*.

D. Modal Decomposition

Once the state matrices (A, B, C) are known, the model parameters in (1) may be computed using a modal (or *eigen*-) decomposition method [52], [53]. If the complex eigenvalues of *A* are assumed to be distinct, one has

$$\lambda\{A\} = \{\lambda_1, \;\; \lambda_2, \;\; \cdots \;\; \lambda_M\}. \tag{28}$$

The magnitude of the eigenvalues $\{\lambda_i\}$ determines amplitude decay/growth rate (with respect to frequency) of the system output, and their phase provides the time delay τ_i or the range R_i in (1). As noted in (11), the eigenvalues of *A* represent the poles of the transfer function, *T(z)*. The eigenvalues $\{\lambda_i\}$ and the eigenvectors $[\psi_i]$ of the state matrix *A* satisfy

$$A\psi_i = \lambda_i \psi_i; \quad i = 1, \cdots, M \tag{29}$$

Now let us form a modal matrix Ψ_i from these eigenvectors by stacking them row-wise:

$$\Psi = [\psi_1 \;\; \psi_2 \;\; \cdots \;\; \psi_M] \tag{30}$$

It follows from (28)-(30) that

$$A\Psi = \Psi\Lambda, \tag{31}$$

$$\Lambda = diag\{\lambda_1 \;\; \lambda_2 \;\; \cdots \;\; \lambda_M\}. \tag{32}$$

Therefore, we may calculate Λ from (31) as

$$\Lambda = \Psi^{-1} A \Psi \tag{33}$$

The entries on its main diagonal are exactly the eigenvalues of the state transition matrix A. Therefore, the modal decomposition approach provides valid information to characterize the target, and it can be used to identify point scatterers embedded in the data set. The IIR approximation,

$\hat{y}(k)$, of the data sequence $y(k)$ can be computed in terms of the state matrices using (16) as

$$\hat{y}(k) = CA^{k-1}B, \quad k = 1, 2, \cdots N. \tag{34}$$

After substituting for A from (31) and realizing that $A^n = \Psi\Lambda^n\Psi^{-1}$, we obtain

$$\hat{y}(k) = C\Psi\Lambda^{k-1}\Psi^{-1}B. \tag{35}$$

The amplitudes of the scatterers in (1) may be computed from (34). Let

$$\Psi^{-1} = \begin{bmatrix} v_1 & v_2 & \cdots & v_M \end{bmatrix}^T \tag{36}$$

where the superscript T denotes matrix transpose. After inserting (30), (32) and (36) into (34), we obtain

$$\hat{y}(k) = \sum_{i=1}^{M} (C\psi_i)(v_i B)\lambda_i^{k-1}, \quad k = 1, \cdots, N \tag{37}$$

Using (1), we deduce that the magnitude and phase of the eigenvalues (poles) are related to the model parameters α_i, τ_i, and R_i, respectively, by

$$\alpha_i = \frac{\log|\lambda_i|}{\Delta f}, \; \tau_i = \frac{\phi_i}{2\pi\Delta f}, \text{ and } R_i = \frac{c\phi_i}{4\pi\Delta f}, \; i = 1, \cdots, M \tag{38}$$

In (38), ϕ_i refers to phase of the eigenvalue λ_i. The amplitudes a_i defined in (1) are then obtained from (37) using these eigenvalues, the corresponding eigenvectors, and the state matrices B and C:

$$a_i = \frac{(C\psi_i)(v_i B)}{(\lambda_i)^{\frac{f_1}{\Delta f}}}; \quad i = 1, \cdots, M. \tag{39}$$

The frequency dependence of the amplitudes and their decay/growth rate is emphasized in (38) and (39).

Next, we discuss the physical interpretation of the state space parameters. The correspondence between the scattered response and its state space representation in terms of complex sinusoids becomes apparent when one compares (1) and (37). The poles λ_i of the transfer function yield the localized scattering centers on the scattering object. As derived in the Appendix, the matrices B and C follow from least squares solution applied to linear systems represented by the observability and controllability matrix, respectively (see (63) and (67)). Therefore, the matrices B and C are directly related to the observability and controllability of the linear system in (34). The *observability matrix* $\tilde{\Omega}$ affects the shape of the natural response of the scattered field (directly proportional to the natural modes or eigenvectors of the state transition matrix A) within a given frequency band. The *controllability* matrix $\tilde{\Gamma}$ limits the effect of an input such as an impulse on the scattering response. In other words, the controllability matrix determines how much of the excitation is coupled to the natural modes of a particular scattering center within the defined bandwidth.

III. Numerical Considerations

A. Estimation of the Model Order

In any spectral estimation problem, selection of model order of the underlying system is a critical issue. The difference between the desired and modeled signal, as defined in (1), is a combination of model mismatch error, measurement error, and noise. If this error is Gaussian distributed, then the minimization of the error criterion in (23) represents the maximum likelihood estimate (MLE) for the ARMA problem [18], [66]. In case of MLE, the Akaike information criterion (AIC) or minimum description length (MDL) criterion are often used for model order determination [67]-[69]. An estimator that yields the true number of signals with probability one as the sample size increases to infinity is said to be "consistent." It has been shown in [68] that MDL is a consistent estimator of order, whereas AIC is inconsistent and often overestimates the model order.

SSM has been used with simulated as well as measured data. In deterministic data modeling such as simulated data where the SNR is quite high, we employ the singular value matrix Σ to estimate model order in the SSM. The large singular values in Σ correspond to strong signal components, while the smaller values are generally attributed to noise. For low noise levels, there is a sharp transition between the large and small singular values. This transition point can be used as an estimate of the model order. At higher noise levels, especially for measured data, the transition from large to small singular values may not be well-defined, making model order estimation more difficult. In this case, probabilistic methods such as AIC and MDL criteria have been used for model order estimation (cf. [33]). No general criterion exists to determine which of these methods gives the "optimal" model order, and none of them provide necessary and sufficient conditions to guarantee that all the required signals are included in the model. It is expedient to consider the underlying physics of the scattering mechanism to guide the determination of the number of scatterers using a combination of these methods, and to examine the goodness of fit for each model order by computing the mean square error in the model [40]. For convenience, the equations to compute AIC and MDL from the singular values, σ_i, of the Hankel matrix approximation, $\tilde{H}$, are summarized below [68].

$$AIC(r) = -2(M-r)N \ln\left(\frac{\prod_{i=r+1}^{M} \sigma_i^{-(M-r)}}{\frac{1}{M-r}\sum_{i=r+1}^{M} \sigma_i} \right) + 2r(2M-r) \tag{40}$$

$$MDL(r) = -(M-r)N \ln\left(\frac{\prod_{i=r+1}^{M} \sigma_i^{-(M-r)}}{\frac{1}{M-r}\sum_{i=r+1}^{M} \sigma_i} \right) + \frac{1}{2} r(2M-r)\ln N \tag{41}$$

In the above, M is the maximum model order in (1) and N is the number of data samples. For a given number r of signals, the term in the parentheses simply denotes the ratio of

geometric mean to arithmetic mean of the smallest $M-r$ singular values, and it is a measure of the error between the truth and the model. The number of signals, i.e., the model order, is determined as the value of $r \in \{1,2,\cdots(M-1)\}$ for which either the AIC or the MDL is minimized [68].

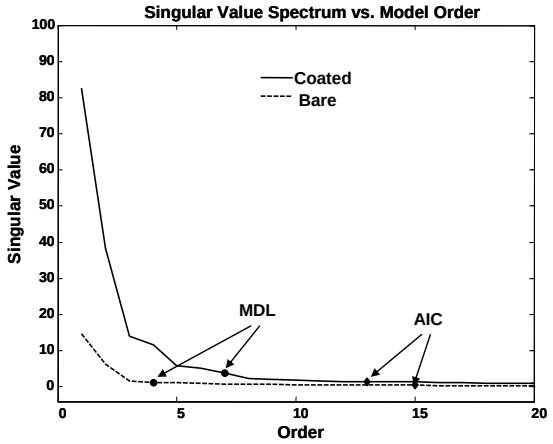

Fig. 1. Singular value spectrum vs. model order for measured RCS on a cone. Circles denote MDL and diamonds denote AIC [40].

As an example, Fig. 1 shows the singular value spectrum (amplitudes in descending order of magnitude) plotted against the model order for experimental RCS data on a right circular conical stationary metallic target with and without a lossy dielectric coating [40]. It is seen that transition from strong signal components to small singular values is not well-defined because of measurement noise. AIC yields an order of 15 and 13 for bare (metallic) and dielectric-coated cones, while MDL yields model orders of 4 and 7, respectively. Due to measurement noise, AIC usually gives a larger estimate than MDL, and modelers usually choose an order no smaller than the AIC prediction. Therefore, an order of 15 has been chosen in [40] to extract the wave features of interest for both metallic and coated cones.

B. Estimation of Signal-to-Noise Ratio

The SNR of the radar system is influenced by noise contributed by several sub-systems, such as oscillator phase noise, mixer *1/f* noise, thermal noise, antenna leakage and mixer leakage. It is cumbersome and often inaccurate to estimate these random noise levels in the radar sub-systems using circuit models [70]. SSM considers this noise through decomposition of the Hankel matrix into signal and noise subspaces using the singular value decomposition.

The threshold for such decomposition is based on the dynamic range and SNR, which can be estimated from power spectrum of the original measured or simulated data, as discussed next. First, we consider measured data on the chest wall displacement of a human subject to extract the heart and respiration rates [41]. UWB radar with a center frequency of 2.4 GHz, bandwidth of 2 GHz and pulse repetition frequency (PRF) of 75 Hz is used to collect the data. The complex signal $I + jQ$ of the radar return from a human subject located 1 m from the radar is plotted in Fig. 2 [41]. Random fluctuations caused by measurement noise are evident. The complex signal in Fig. 2 is transformed with FFT using a Hamming window to suppress the sidelobes. This does not affect the peak signal but clearly defines the noise floor relative to the peak. Therefore, the dynamic range and SNR can be estimated from the compressed (or transformed) signal plotted as a function of Doppler frequency proportional to the chest wall displacement. Fig. 3 shows that the SNR for Channel 3 data is moderately high (around 24 dB), as one may expect from indoor laboratory RCS measurements, which are not subject to multipath and clutter encountered by fielded radar systems. Next, we consider SNR evaluation for simulated data.

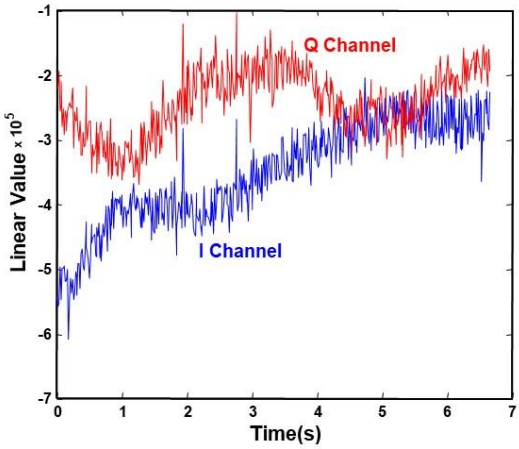

Fig. 2. Raw time sequences of I and Q channels [41].

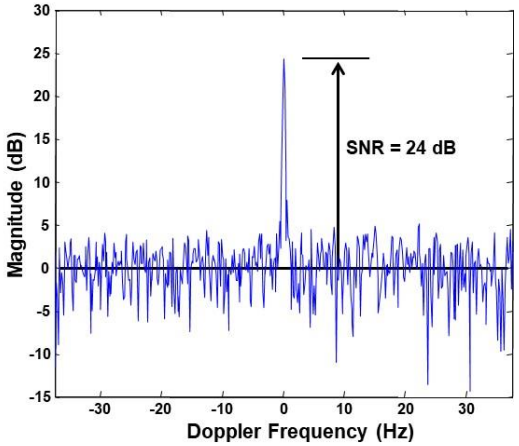

Fig. 3. SNR estimate from UWB radar data on a human subject [41].

In simulated data, the difference between the desired and the modeled signal, as defined in (1), is a combination of model mismatch error and any noise intentionally added to the signal to determine statistical effects of random variation in parameters (e.g., Monte Carlo trials). In the absence of any added noise, the model mismatch error can be treated as noise. The SNR can be defined as the ratio of variance of the signal data sequence to the variance of the noise sequence,

$$SNR = 10\log\left(\frac{V\{\hat{y}(k)\}}{V\{y(k)-\hat{y}(k)\}}\right),\ k = 1,2,\cdots,N \qquad (42)$$

where *V* stands for variance defined by

$$V\{f(k)\} = \frac{1}{N-1}\sum_{k=1}^{N}\left|f(k)-\mu\right|^2, \qquad (43)$$

and μ is the mean of $f(k)$, given by

$$\mu = \frac{1}{N}\sum_{k=1}^{N} f(k). \tag{44}$$

In a noise-free situation, if the SSM estimates defined by (34) closely match the data samples, the SNR defines the *dynamic range* of the model. Thus, the number of scatterers or signals giving rise to the estimates corresponds exactly to the number of sinusoids embedded in the data. In a noisy situation, it is important to use caution so that the estimates are not direct replicas of the noisy samples. Therefore, an "optimal" model order should provide appropriate SNR or dynamic range for a sinusoid being modelled.

IV. Results and Discussion

In this section, two examples based on *simulated data* are presented to illustrate the state space method. In the first example, we consider a planar dielectric slab illuminated by a plane wave at normal incidence and isolate the reflection off the front face using range-classified poles pertinent to the specular reflection. The subsequent radar-return signals enable classification of multiple internal reflections also. In the second example, we consider Mie scattering from a sphere in the absence of noise, extract the creeping wave that circumnavigates the shadow zone and returns to the radar, and examine accuracy of the SSM estimates by comparison with an analytically derived expression of the creeping wave. Next, random white Gaussian noise is added to the Mie series solution, and Monte Carlo simulation is performed to examine robustness of the estimates to noise. Numerical considerations such as SNR, singular value spectrum and order determination are addressed in detail for both of these examples. The reader is referred to [40]-[43] for application of SSM to feature identification using monostatic RCS *measured data* on stationary targets as well as human subjects.

A. Reflection by a Dielectric Slab

Plane wave reflection from a 15-mm thick lossy dielectric slab with dielectric constant $\varepsilon_r = (5, -0.01)$ is considered, and it is shown that the response of the front face of the slab as well as multiple internal reflections can all be isolated from the composite response using SSM. Each of these contributions is specifically mapped to a range-gated pole. The slab of thickness d is located in free space. Its Fresnel reflection coefficient is calculated as

$$y(\omega) = \Gamma = \frac{\left(\eta_1^2 - \eta_0^2\right)\tanh\left(\gamma_1 d\right)}{2\eta_1\eta_0 + \left(\eta_1^2 + \eta_0^2\right)\tanh\left(\gamma_1 d\right)}, \tag{45}$$

$$\gamma_1 = jk_1, \quad k_1 = k_0\sqrt{\varepsilon_r}, \quad k_0 = \omega\sqrt{\mu_0\varepsilon_0}, \qquad \eta_1 = \eta_0/\sqrt{\varepsilon_r}, \quad \eta_0 = 120\pi. \tag{46}$$

Without loss of generality, normal incidence is considered for illustration. The complex propagation constant and intrinsic impedance in the lossy dielectric are given by γ_1 and η_1, respectively. The phase constant and the intrinsic impedance of free space are denoted as k_0 and η_0, respectively, while ω is the angular frequency. The reflection coefficient is calculated at normal incidence over 2-20 GHz bandwidth and Fourier transformed, using a Hamming window to suppress the sidelobes, to obtain the composite response shown in Fig. 4. The transform employs distance to the scatterer (or *range*) instead of time, an operation known as *pulse compression*.

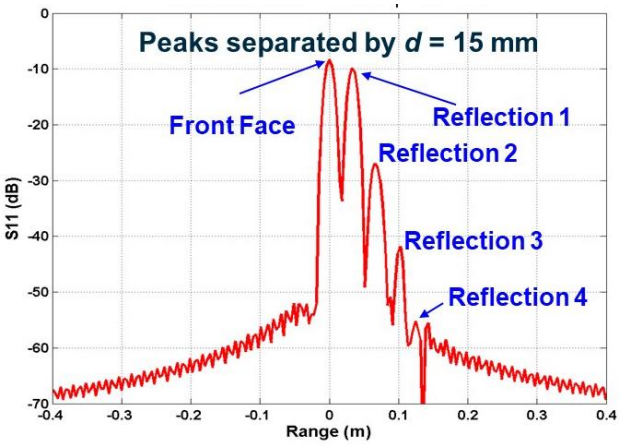

Fig. 4. Range response of the 15-mm thick slab reflection coefficient.

Because the phase reference is at the front face, the pulse with peak at zero range is the reflection off the slab-front, the second pulse is the first reflection off the back face arriving coherently at the "receiver," the third pulse is the second re-reflection off the back, and so on, as illustrated geometrically in Fig. 5 using transmission line analogy [71].

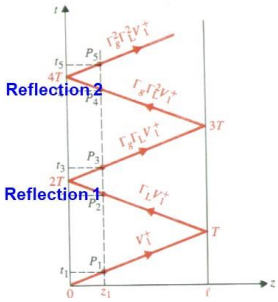

Fig. 5. Reflection diagram in analogy with transmission line circuit [71].

Next, a 10th order state-space model (see (1)) is estimated from the simulated data. The model parameters are listed in Table 1, where the poles and the signal amplitudes are classified in terms of scatterers of interest highlighted in the last column. The rows are sorted in descending order of the peak amplitude. All the poles lie within or on the unit circle, validating the stability of the system.

Table 1. SSM parameters for model order M = 10.

Index	Pole Location	Complex Amplitude	Abs(Amp)	Range (m)	Notes
1	1.0000 - j0.0000	-0.3820 + j0.0004	0.381967	0.0000	Front
2	1.0000 - j0.0070	-0.3077 - j0.1057	0.325323	0.0150	Refl. 1
3	0.9999 - j0.0140	0.0374 + j0.0290	0.047331	0.0300	Refl. 2
4	0.9998 - j0.0211	-0.0038 - j0.0058	0.006886	0.0450	Refl. 3
5	0.9996 - j0.0281	0.0002 + j0.0010	0.001002	0.0600	Refl. 4
6	0.9993 - j0.0351	0.0000 - j0.0001	0.000146	0.0750	Refl. 5
8	0.9991 - j0.0421	0.0000 + j0.0000	0.000021	0.0900	
9	0.9987 - j0.0492	0.0000 - j0.0000	0.000003	0.1050	
10	0.9984 - j0.0562	0.0000 + j0.0000	0.000000	0.1200	
7	0.9979 - j0.0632	0.0000 - j0.0000	0.000000	0.1350	

It is interesting that the signal peaks are separated in SSM-computed range (see (38)) by exactly 15 mm, the thickness of

the slab. The dominant pole, located at (1, 0) with amplitude of 0.382 and phase π, is found to have zero range. This signal corresponds to the isolated front face reflection. The subsequent poles, consecutively spaced at 15 mm, represent the isolated secondary reflections off the back face, as illustrated in Fig. 4. The first five signals of interest in Table 1 appear to have the maximum spectral content, as the sixth term is three orders of magnitude smaller than the dominant signal. Using the coherent summation of only these first five terms in the state space model (1), we have computed the frequency response of the composite signal. Fig. 6 compares the "truth" with the state space model in both magnitude and phase, and the two sets of curves overlap each other, signifying excellent model fidelity.

As alluded, one can isolate the front face response by using only the dominant pole at zero range. The reflection coefficient of this isolated pulse is the same as that of the half-space problem because the delayed reflections off the back face are not included. Therefore, using the constant amplitude of $\Gamma_f = -0.382 + j0.004$ from Table 1, the slab's dielectric constant can be determined as

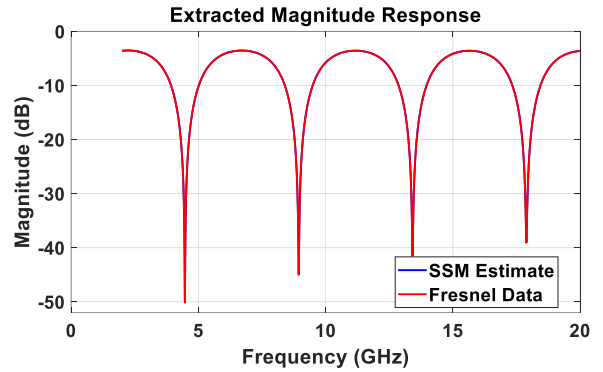

(a)

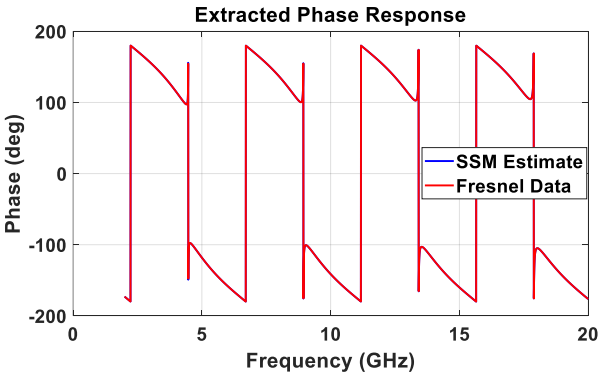

(b)

Fig. 6. Corroboration between SSM model and the truth (eq. (45)) using only the first five signals in Table 1. (a) Magnitude, (b) Phase.

$$\varepsilon_r = \left(\frac{1-\Gamma_f}{1+\Gamma_f} \right)^2 . \qquad (47)$$

Eq. (47) yields $\varepsilon_r = 5 - j0.01$ *exactly*, verifying the accuracy of the signal extraction. It is imperative that isolation of individual signals of interest requires adequate bandwidth to provide the spectral resolution needed to separate the peaks.

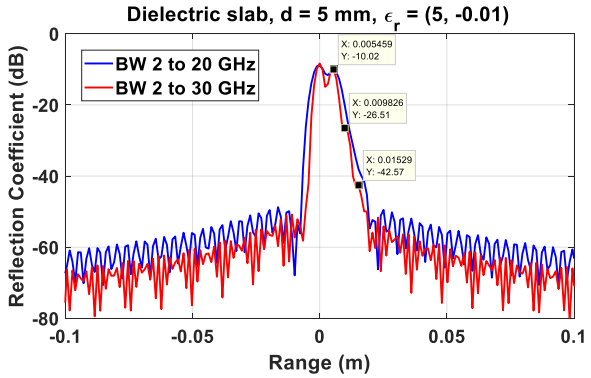

Fig. 7. Range response of the 5-mm thick slab reflection coefficient.

When the thickness of the slab is reduced to 5 mm, one obtains the compressed range response shown in Fig. 7, which clearly shows the impending merging of the first two peaks. Using a bandwidth of 18 GHz, these two peaks are very close in amplitude, and may not be adequately resolved in range. But when the bandwidth is increased to 28 GHz, the peaks can be isolated. Furthermore, in the latter case, the markers also indicate secondary fluctuations appearing at approximately 10 and 15 mm, corresponding to re-reflections off the back face. However, in measured data, such small fluctuations of the main lobe may be masked by noise, and a larger bandwidth may not necessarily improve the SNR.

Fig. 8 plots the model error magnitude of the frequency-domain response for SSM with order M = 5 (the first five terms in Table 1) and d = 15 mm. The mean error is -77.3 dB, proving that all the significant signals have been modeled. A similar agreement between raw data and SSM is observed in the phase too, with mean error of 0.2°.

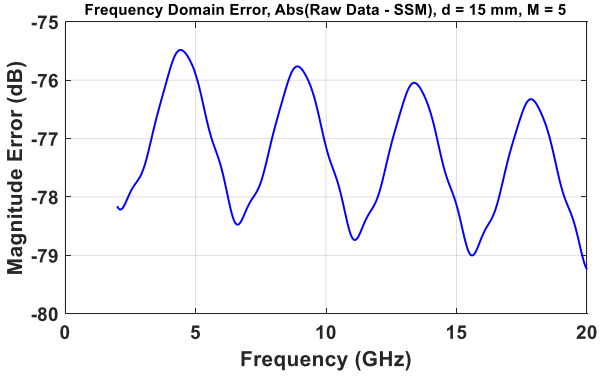

Fig. 8. Model error in magnitude of the SSM frequency response.

The model error for M = 10 and M = 15 did not decrease beyond the error depicted in Fig. 8 for M = 5. A performance measure for evaluation of the model error is the SNR in (42). Table 2 lists the SNR for few model orders ranging from 5 to 15. It is evident that SSM with M = 10 gives the highest SNR and any further increase in the order does not impact the error.

Table 2. SNR as a function of model order for the slab problem.

Model Order	5	10	15
SNR (dB)	67.4	101.1	101.1

A deeper understanding of the sources of modeling error in SSM can be obtained by examining the error for various

model orders relative to the compressed SSM signal. Along with the singular value spectrum, to be discussed shortly, this will help us in evaluating impact of the signals discarded in the model as "noise." Fig. 9 displays the error responses for model orders M = 5 and M = 10, compressed using a 4,096-point FFT on sequences of length 3,601, with a Hamming window to suppress the noise sidelobes. For comparison, the compressed SSM signal estimate, identical for the two model orders, is also shown. The range coordinate for each peak (in mm) is annotated in the graph. We observe that the SSM signal, $\hat{y}(k)$, models the five dominant reflections signified by the first five poles (see Table 1), and the remaining signals are embedded in noise. Because these discarded signals are there in the truth data (45), it is not surprising that the range spectra of the error signal, $y(k)-\hat{y}(k)$, depict these discarded noise peaks precisely. The number of such noise peaks embedded in the error sequence depends on the model order. For example, with M = 5, we calculate a noise floor of -110 dB (the mean square of the compressed error pulse) and identify the three noise peaks at 75, 90 and 105 mm. With M = 10, we can identify the noise peaks at 105, 120 and 135 mm.

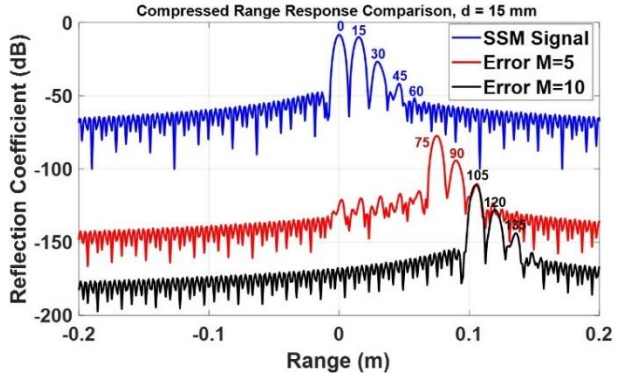

Fig. 9. Comparison of the compressed signal and noise (error) responses for two model orders. The numbers above each peak indicate the range in mm.

The noise spectrum did not change with any further increase in model order beyond 10. Thus, the last noise peak one can identify is at 135 mm. As the highest noise peak (at 75 mm) is 90 dB down from the main reflection at zero range, none of these discarded noise peaks has any influence on the SNR.

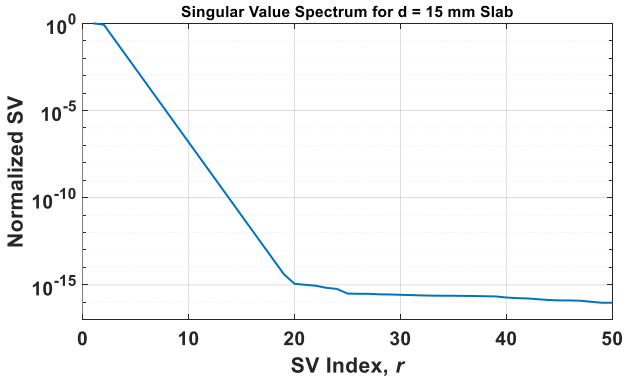

Fig. 10. Singular value spectrum to determine the model order.

Lastly, we estimate the model order by examining the singular value spectrum plotted in Fig. 10 as a function of its index, r. The SVs are normalized to the largest value ($r=1$). The model order can be determined subject to the threshold [56] $\sigma_r/\sigma_1 \approx 10^{-p}$, where p is the number of significant decimal places in the truth data. Thus, if the data is accurate to 7 places, the SV spectrum predicts a model order of $r=10$. In practice, the data may be accurate to third or fourth decimal place, but not till the seventh as the simulated reflection coefficient (45) for this simple illustrative problem. For three-digit accuracy, Table 1 indicates that a model order of 10 yields 5 signal poles and 5 noise poles (weak signals embedded in noise). Indeed, the error analysis in Figs. 8 and 9 validates this observation.

B. Scattering by a Sphere

Let us consider the extraction of creeping waves from the canonical problem of scattering by a perfect electrically conducting (PEC) sphere using the SSM. The scattered field for plane wave incidence is computed analytically using the Mie series [72], first in the absence of noise, and then with the influence of additive Gaussian noise. The model order is estimated in each case by examining the singular value spectrum, and the accuracy of the extracted creeping wave is established by comparison with an analytically derived asymptotic expression of the creeping wave [73].

B.1. Baseline without Noise

The monostatic RCS is calculated for a PEC sphere of radius $a=17.7$ cm using the Mie series, and is plotted against frequency over a range of 2 to 20 GHz in Fig. 11. As the radius becomes much larger than the wavelength, the normalized RCS asymptotically approaches πa^2. The contribution to back-scattered field comes from a specularly reflected ray emanating from point *A*, and a creeping wave, which attaches to the sphere tangentially at point *B*, navigates half the circumference, and detaches at the symmetrical tangential location *C*, as shown in the inset in Fig. 11. The specular contribution is governed by geometrical optics (GO) approximation and can be analytically calculated [74]. The creeping wave diffracted field can be approximated by asymptotic evaluation of the Fock integrals [73], [74].

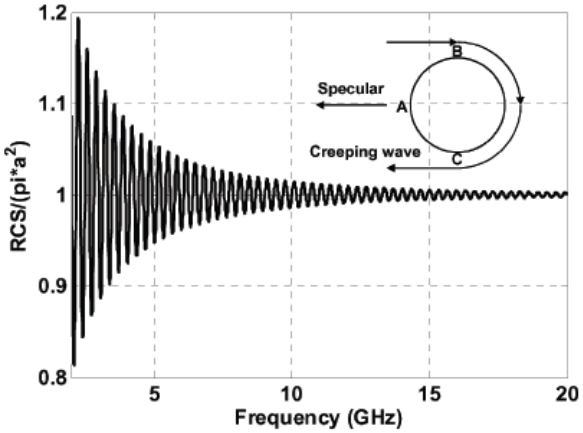

Fig. 11. Normalized RCS of a PEC sphere, computed using Mie series.

In order to isolate the scattering centers pertinent to the specular and the creeping wave, we first compute the range

profile of the back-scattered field, displayed in Fig. 12, by FFT of the Mie series frequency response using a Hamming window to suppress the sidelobes. The phase reference is chosen such that the point of specular reflection is at zero range. The second peak which corresponds to the creeping wave is at 0.454 m range, in agreement with the range predicted from ray path geometry (see the inset of Fig. 11) as 0.455 m, i.e., $R = (\pi/2+1)a$.

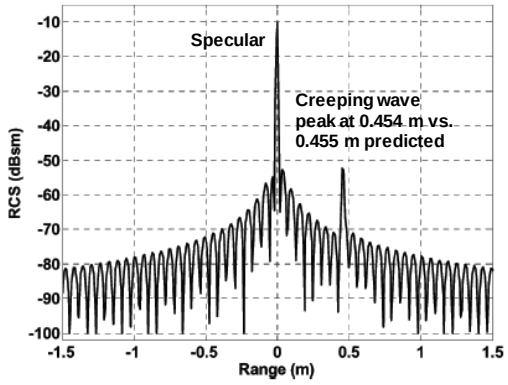

Fig. 12. Range profile of the back-scattered field.

Next, SSM is applied to extract range-isolated poles specific to the creeping wave, and their cumulative frequency response is calculated. A 10th order state space model is computed from the Mie series frequency response shown in Fig. 11. We have observed excellent corroboration between the estimated SSM model and the truth data in Fig. 11 over the entire 18 GHz band. For brevity, we focus only on representation of the creeping wave using the corresponding range-isolated poles from the SSM. As described in Section II, an advantage of using range processing with the spectral estimation method is the direct relation between range and pole phase (see (38)). Thus, one may isolate a given scattering mode by adding contributions from *only* the poles associated with the range window of that mode. Of the 10 poles used in the SSM to represent the entire signal in Fig. 11, only two poles are identified with model-computed range of 0.454 m, relevant to the creeping wave peak. By coherently summing the contributions of only these two poles, we obtain the extracted frequency response shown in Fig. 13.

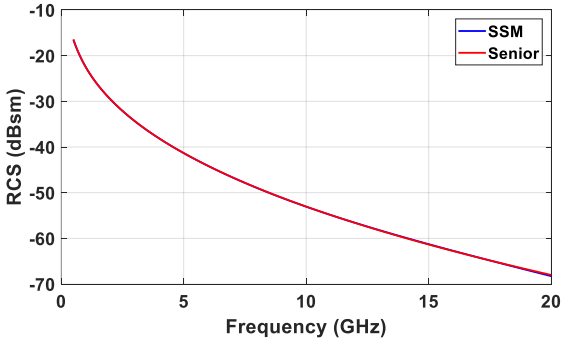

Fig. 13. Comparison of SSM-extracted creeping wave with the analytical solution from [73].

In order to demonstrate baseline validation with no noise present in the data, we also plot in Fig. 13 an analytical solution for the spherical creeping wave from [73], which essentially overlaps with the SSM-estimated data. The signal amplitudes for the two creeping wave poles are observed to be around -36 dB, signifying high accuracy in the model even for small signals. Later, we will evaluate model robustness using Monte Carlo analysis with Gaussian noise added to the Mie series. The absolute model prediction error for the creeping wave estimation is plotted in Fig. 14. A similar agreement with the analytical solution is also observed for the specular peak extracted from the Mie series in Fig. 11.

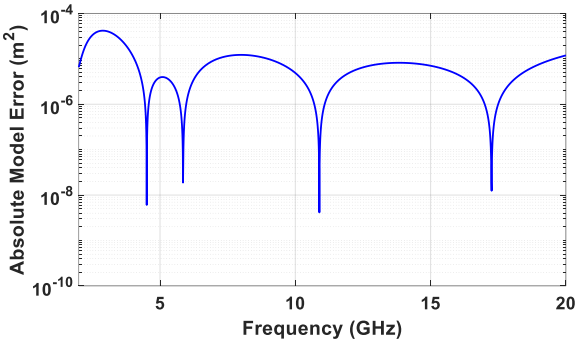

Fig. 14. Model prediction error for the extracted creeping wave relative to the analytical solution from [73].

B.2. Monte Carlo Analysis

The SSM extraction of signals of interest from Mie series in the presence of noise is considered next. Monte Carlo (MC) analysis is performed by adding random noise of a given SNR to the Mie series solution for the PEC sphere and evaluating the accuracy of the SSM-extracted components, namely, the creeping wave and the specular. The measurement noise *w(k)* (see (1)) is assumed to be complex white Gaussian with variance σ_n^2, defined by peak signal-to-noise ratio

$$SNR = 20\ \log\left(\frac{\sigma_{sn}}{\sigma_n}\right), \qquad (48)$$

where σ_{sn}^2 denotes the signal variance. For a given SNR, 1000 independent trials are executed on the Mie series solution, and the state space method is applied to process each noise-corrupted data sequence and extract the wave constituents of interest. In order to assess the quality of the data, the noise-corrupted Mie series (truth) data is plotted in Fig. 15 against SSM model (with order M = 10) of the *total response* for the mean of 1000 MC trials with SNR = 20 dB. It is observed that coherent averaging of the MC trials reduces the influence of noise considerably. As the electrical size of the sphere increases, the asymptotic limit of SSM correctly reaches πa^2.

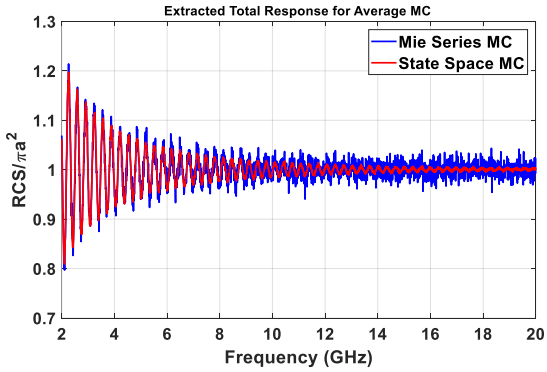

Fig. 15. Average of the SSM-extracted Mie series composite signal over 1000 Monte Carlo trials.

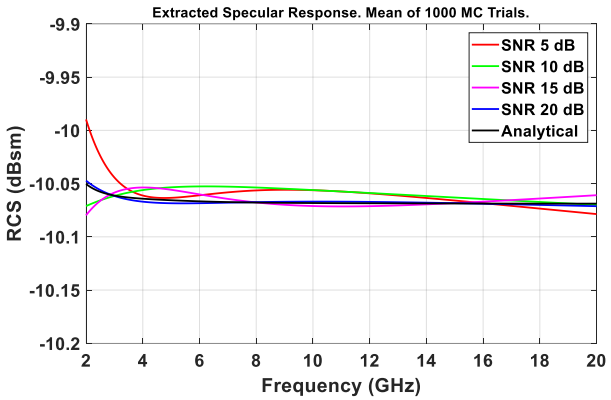

Fig. 16. Average of the SSM-extracted specular wave signal over 1000 Monte Carlo trials.

Next, we consider the extraction of the specular wave. Fig. 16 depicts the frequency response corresponding to SSM processing of the average of 1000 MC trials, with SNR ranging from 5 dB to 20 dB. Only two poles are used in the SSM for the extraction. The response for each SNR is observed to track the analytical (noise-free) solution quite well. The worst-case error relative to the reference solution is about 0.05 dB and occurs for *SNR* = 5 dB. More importantly, because of the relatively large amplitude of the specular (about -10 dB), we have observed good correlation between corresponding pole locations for each trial. For brevity, the pole plots are not included.

We address Monte Carlo analysis of the creeping wave next. As seen in Fig. 13, the noise-free creeping wave signal has an amplitude of -20 to -70 dB, and therefore, adding noise before the creeping wave extraction would considerably stress the state space algorithm. Fig. 17 displays the performance of SSM in extracting the creeping wave for various SNRs, relative to the reference analytical solution from [73].

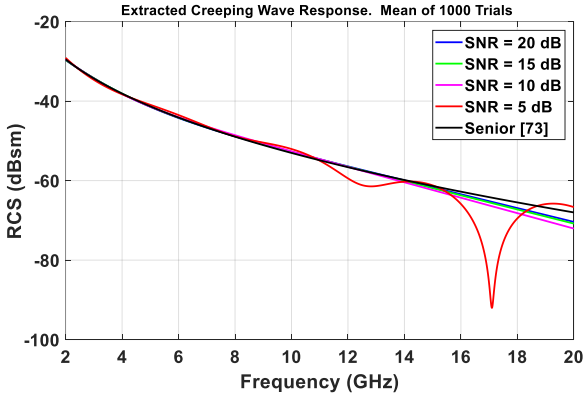

Fig. 17. Comparison of SSM-extracted creeping wave for the average of 1000 MC trials with the analytical solution from [73].

The extracted signal is in reasonable agreement with the analytical solution for $SNR \geq 10$ dB. The SSM estimate deviates significantly from the reference solution at frequencies greater than 10 GHz for *SNR* = 5 dB. For SNRs between 5 and 15 dB, the error increases with frequency for $f > 16$ GHz, but the RCS response is around -70 to -65 dB, which is approaching the noise floor. It has been observed that the pole drift from trial to trial becomes significant for *SNR* = 5 dB, and in fact, for signals smaller than -60 dB, it becomes difficult to discriminate noise poles from the signal poles. Therefore, for weak signals such as creeping waves, caution should be exercised in extracting the signal under low SNR conditions. Nevertheless, the worst-case performance of SSM under the stressing conditions depicted in Fig. 17 is gratifying, given that the frequency response of the creeping wave signal for each SNR, extracted from the average of 1000 MC trials of the Mie series, follows the overall analytical trend. One can improve the noise performance by employing two-dimensional data, e.g., aspect- and frequency-dependent RCS, which improves the SNR by coherent integration of frequency samples over many pulses [61], [62]. Our extensive work on state-space methods to process biomedical radar data [41]-[43], [75], [76] suggests that the SNR of vital sign detection can be substantially improved, and additional features such as subject localization, motion compensation, gait analysis, etc., can be estimated, using block-processing of one-dimensional data (in the frequency domain) to attain considerably improved accuracy over FFT-based methods.

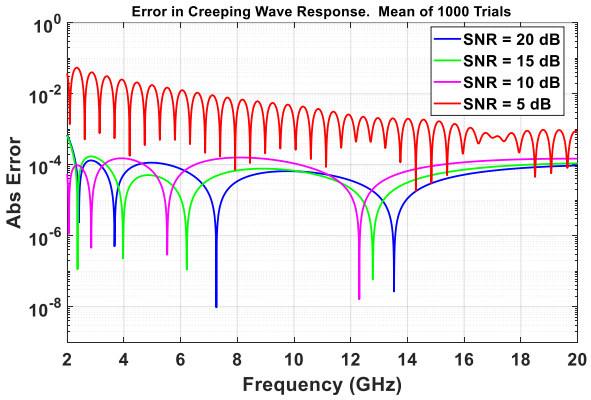

Fig. 18. Model prediction error for the extracted creeping wave relative to the analytical solution from [73] after 1000 MC trials.

The absolute model prediction error for the creeping wave estimation from the average of 1000 MC trials on the Mie series is plotted in Fig. 18 in terms of the SNR. It is evident that the worst-case error for *SNR* = 5 dB is between two to four orders of magnitude larger than the model error for the noise-free case shown in Fig. 14. For $SNR \geq 10$ dB, the error is only slightly larger than that in Fig. 14.

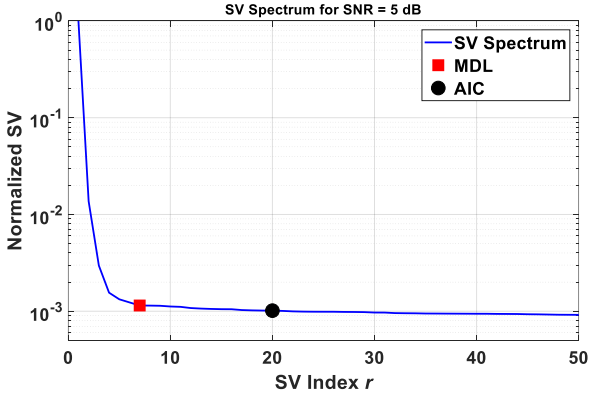

Fig. 19. Singular value spectrum vs. model order for noisy data with SNR = 5. MDL yields a model order of 7 and AIC, an order of 20.

Lastly, we investigate the model order by computing the singular value spectrum as well as AIC and MDL estimates.

It is seen in Fig. 19 that the transition from strong signal components to small singular values is not well-defined because of noise. AIC yields model order of 20 while MDL yields 7. Due to measurement noise, AIC usually gives a larger estimate than MDL, and modelers usually choose an order no smaller than the AIC prediction. Therefore, an order of 20 has been chosen to extract the wave features of interest for the sphere. Compared to estimates in the dielectric slab case, which have a very high SNR (see Table 2), the accuracy in the SSM estimate for the MC trials is much lower, of the order 0.001.

V. CONCLUSIONS

A spectral model based on state-space ARMA representation has been presented to isolate and extract modal EM responses, such as creeping waves and multiply reflected or diffracted waves, which are of interest in radar target identification and feature extraction. The eigenvalues of the open-loop system matrix, i.e., poles of the ARMA transfer function, provide the range and the *frequency-dependent* amplitude decay/growth rate of the field data. The amplitudes in the complex exponential model are obtained by least squares modal decomposition involving the state matrices. Range classification of the poles allows for isolation of desired responses in the EM signature via pulse compression and spectral decomposition. For purposes of illustration, in this paper the SSM is reviewed by application to two simple EM problems, namely, Fresnel reflection by a dielectric slab and the extraction of creeping waves using Mie scattering by a PEC sphere. The method has been applied to isolate the leading-edge reflection and multiple internal reflections of the slab. It is shown that range-classification of the singularities in the response enables characterization of the isolated reflected waves using a low model-order SSM representation. In the second example, we have analyzed the extraction of creeping waves from Mie scattering by a PEC sphere in the absence of noise. The SSM estimates of the extracted creeping wave have been validated by comparison with an analytically derived expression of the creeping wave. Next, random white Gaussian noise is added to the Mie series solution, and Monte Carlo simulation is performed to examine robustness of the SSM estimates to noise. Numerical considerations such as SNR, singular value spectrum and order determination are addressed in detail for both of these examples. The reader is referred to [40]-[43] for application of SSM to feature identification using monostatic RCS *measured data* on stationary targets as well as human subjects. As we have shown in [40], the isolation of electromagnetic wave species of interest, such as creeping waves, multiply diffracted waves and specular scattering, yields a better understanding of the physics behind wave propagation around curved dielectric or coated structures, thereby improving the accuracy of feature extraction or target identification.

APPENDIX

In terms of the finite-rank observability matrix $\tilde{\Omega} \in \mathbf{C}^{(N-L+1)\times M}$ computed from the SVD in (25) as

$$\tilde{\Omega} = \begin{bmatrix} C & CA & CA^2 & \cdots & CA^{N-L-1} & CA^{N-L} \end{bmatrix}^T, \quad (49)$$

the state transition or the open-loop matrix $A \in \mathbf{C}^{M\times M}$ is determined by the solution to the matrix equation

$$\tilde{\Omega}_{-r\ell} A = \tilde{\Omega}_{-r1}, \quad (50)$$

with

$$\tilde{\Omega}_{-r1} = \begin{bmatrix} CA & CA^2 & CA^3 & \cdots & CA^{N-L} \end{bmatrix}^T, \quad (51)$$

$$\tilde{\Omega}_{-r\ell} = \begin{bmatrix} C & CA & CA^2 & \cdots & CA^{N-L-1} \end{bmatrix}^T. \quad (52)$$

It is observed that the matrices $\tilde{\Omega}_{-r1}$ and $\tilde{\Omega}_{-r\ell}$ are obtained by deleting the first and last rows, respectively, of the matrix $\tilde{\Omega}$ in (49). Using the pseudo-inverse least squares on (50), we obtain the state transition matrix *A* given in (26) and repeated below.

$$A = \left(\tilde{\Omega}^*_{-r\ell}\tilde{\Omega}_{-r\ell}\right)^{-1}\tilde{\Omega}^*_{-r\ell}\tilde{\Omega}_{-r1}. \quad (53)$$

This matrix may also be derived from the controllability matrix $\tilde{\Gamma} \in \mathbf{C}^{M\times L}$ derived from the SVD in (25) as

$$\tilde{\Gamma} = \begin{bmatrix} B & AB & A^2B & A^3B & \cdots & A^{L-1}B \end{bmatrix}. \quad (54)$$

It follows that the state transition matrix *A* satisfies the matrix equation

$$A\tilde{\Gamma}_{-c\ell} = \tilde{\Gamma}_{-c1}, \quad (55)$$

with

$$\tilde{\Gamma}_{-c1} = \begin{bmatrix} AB & A^2B & A^3B & \cdots & A^{L-1}B \end{bmatrix}, \quad (56)$$

$$\tilde{\Gamma}_{-c\ell} = \begin{bmatrix} B & AB & A^2B & \cdots & A^{L-2}B \end{bmatrix}. \quad (57)$$

Eqs. (56) and (57) are obtained by deleting the first and last columns, respectively, of the controllability matrix $\tilde{\Gamma}$ in (54). By solving (55) for *A* using the pseudo-inverse least squares method, equivalent to (53), we obtain (also see (27))

$$A = \tilde{\Gamma}_{-c1}\tilde{\Gamma}^*_{-c\ell}(\tilde{\Gamma}_{-c\ell}\tilde{\Gamma}^*_{-c\ell})^{-1}. \quad (58)$$

Next, we address the computation of control and observation matrices, *B* and *C*, respectively, using *two alternative approaches*. In the first approach, it follows from (49) that the observation matrix *C* is simply given by the first row of the observability matrix,

$$C = \tilde{\Omega}(1,:). \quad (59)$$

Alternatively, the IIR approximation, $\hat{y}(k)$, of the data sequence $y(k)$, $k = 1, 2, \cdots N$, can be computed in terms of the state matrices using (16) as

$$\hat{y}(k) = CA^{k-1}B, \quad k = 1, 2, \cdots N. \quad (60)$$

We define the *augmented* observability matrix employing all the *N* samples:

$$\tilde{\Omega}_N = \begin{bmatrix} C & CA & CA^2 & \cdots & CA^{N-1} \end{bmatrix}^T, \quad (61)$$

which is related to the impulse response in (60) as

$$\tilde{\Omega}_N B = \hat{y}^T. \quad (62)$$

Therefore, in order to minimize the error between the model $\hat{y}$ and the measured data vector y, the control matrix B is computed by the pseudo-inverse least squares method, as shown below.

$$B = \left(\tilde{\Omega}_N^* \tilde{\Omega}_N\right)^{-1} \tilde{\Omega}_N^* \hat{y}^T. \tag{63}$$

In summary, in the first approach, one may calculate the matrices C and B from the observability matrix $\tilde{\Omega}$, using (59) and (63), respectively.

Alternatively, in the second approach, B is computed from the first column of the controllability matrix in (54) as

$$B = \tilde{\Gamma}(:,1). \tag{64}$$

and C follows from the least squares fit between the data sequence $y(k)$, and the state-space IIR approximation $\hat{y}(k)$ in (60), as shown next. In terms of the *augmented* controllability matrix

$$\tilde{\Gamma}_N = \begin{bmatrix} B & AB & A^2B & \cdots & A^{N-1}B \end{bmatrix}, \tag{65}$$

the estimation problem for C may be written as

$$C\tilde{\Gamma}_N = \hat{y}, \tag{66}$$

and its pseudo-inverse least squares solution yields

$$C = \hat{y}\tilde{\Gamma}_N^* (\tilde{\Gamma}_N \tilde{\Gamma}_N^*)^{-1}. \tag{67}$$

To summarize, it is emphasized that there are two expressions for the state transition matrix, A, and two corresponding alternative approaches to computing B and C. The matrix A may be computed from either the observability matrix using (53), or the controllability matrix using (58). Correspondingly, the matrices B and C must be computed by using either (63) and (59), or (64) and (67), respectively. In order to improve the estimation accuracy in a low SNR environment, we almost always employ the least-squares computations (63) and (67) to estimate B and C, respectively, and seldom use (64) and (59).

REFERENCES

[1] R. F. Harrington, Field *Computation by Moment Methods*, New York, NY: Macmillan, 1968.

[2] J. Jin, *The Finite Element Method in Electromagnetics*, New York, NY: John Wiley, 1992.

[3] A. Taflove, *Computational Electrodynamics: The Finite-Difference Time-Domain Method*, Boston, MA: Artech House, 1995.

[4] W. J. R. Hoefer, "The transmission-line matrix method – theory and applications," *IEEE Trans. Microwave Theory Tech*., vol. 33, no. 10, pp. 882-893, Oct. 1985.

[5] Baron de Prony, Gaspard-Clair-Fran¸cois-Marie Riche, "Essai experimental et analytique sur les lois de la Dilatabilité des fluides élastiques et sur celles de la Force expansive de la vapeur de l'eau et de la vapeur de l'alcohol, à differerentes temperatures," *J. de l'Ecole ´Polytechnique*, 1 (1795), 24–76.

[6] S.M. Kay and S.L. Marple, "Spectrum analysis – a modern perspective," *Proc. IEEE*, vol. 69, no. 11, pp 1380-1419, Nov.1981.

[7] V. K. Jain, "Filter analysis by use of pencil-of-functions: Part 1," *IEEE Trans. Circuits Syst.*, vol. CAS-21, pp. 574-579, Sept. 1974.

[8] V. K. Jain, "Filter analysis by use of pencil-of-functions: Part 2," *IEEE Trans. Circuits Syst.*, vol. CAS-21, pp. 580-583, Sept. 1974.

[9] V. K. Jain, T. K. Sarkar, and D. D. Weiner, "Rational modeling by pencil-of-functions method," *IEEE Trans. Acoust., Speech, Signal Processing*, vol. ASSP-31, pp. 564-573, June 1983.

[10] K. Ogata, *Discrete-Time Control Systems*, New York: Prentice-Hall, 1987.

[11] Y. Hua and T. K. Sarkar, "Matrix pencil method for estimating parameters of exponentially damped/undamped sinusoids in noise," *IEEE Trans. Acoust. Speech, Signal Processing*, vol. 38, no. 5, pp. 814–824, 1990.

[12] J.A. Cadzow, "Spectral estimation: An overdetermined rational model equation approach," *Proc. IEEE*, vol. 70, no. 9, pp. 907-939, Sept. 1982.

[13] A. K. Shaw, "A decoupled approach for optimal estimation of transfer function parameters from input–output data," *IEEE Trans. Signal Processing*, vol. 42, pp. 1275–1278, May 1994.

[14] A**.** Paulraj, R. Roy, and T. Kailtath, "Estimation of signal parameters via rotational invariance techniques-ESPRIT," in *Proc. Nineteenth Ann. Asilomar Conference on Circuits, System**, and Computers*, Pacific Grove, CA, pp. 83-89, Nov. 1985.

[15] R. Roy, A**.** Paulraj, and T. Kailath, "ESPRIT-A subspace rotation approach to estimation of parameters of cisoids in noise," *IEEE Trans. Acoust., Speech, Signal Processing*, vol. ASSP-34, pp. 1340-1342, Oct. 1986.

[16] R. Roy and T. Kailath, "ESPRIT-Estimation of signal parameters via rotational Invariance techniques," *IEEE Trans. Acoust., Speech, Signal Processing*, vol. ASSP-37, pp. 984-995, July 1989.

[17] R. O. Schmidt, "Multiple emitter location and signal parameter estimation," *IEEE Trans. Antennas Propagat.*, vol. AP-34, pp. 276-280, March 1986.

[18] S. Y. Kung, K. S. Arun, and D. V. Bhaskar Rao, "State-space and singular value decomposition-based approximation methods for the harmonic retrieval problem," *J. Optical Society of America*, vol.73, no. 12, pp. 1799-1811, December 1983.

[19] J. J. Fuchs, "State-space modeling and estimation of time differences of arrival,'' *IEEE Trans. Acoust., Speech, Signal Processing*, vol. ASSP-34, pp. 232-244, Apr. 1986.

[20] M. Aoki, *State Space Modeling* of *Time Series*. New York: Springer Verlag, 1987.

[21] B. D. Rao and K. S. Arun, "Model based processing of signals: a state space approach," *Proc. IEEE,* vol. 80, no. 2, pp. 283-309, Feb. 1992.

[22] M. L. Van Blaricum and R. Mittra, "A technique for extracting the poles and residues of a system directly from its transient response," *IEEE Trans. Antennas Propagat.*, vol. AP-23, pp. 777-781, November 1975.

[23] M. P. Hurst and R. Mittra, "Scattering center analysis via Prony's method," *IEEE Trans. Antennas Propagat.*, vol. AP-35, pp. 986-988, August 1987.

[24] A. J. Mackay and A. McCowen, "An improved pencil-of-functions method and comparisons with traditional methods of pole extraction," *IEEE Trans. Antennas Propagat*., vol. AP-35, no. 4, pp. 435-441, April 1987.

[25] Y. Hua and T. K. Sarkar, "Generalized pencil-of-functions method for extracting poles of an EM system from its transient response," *IEEE Trans. Antennas Propagat.*, vol. AP-37, no. 2, pp. 229-234, February 1989.

[26] Y. Hua and T.K. Sarkar, "Matrix pencil method for estimating parameters for exponentially damped/undamped sinusoids in noise," *IEEE Trans. Accoust. Speech, Signal Processing*, vol. 36, no. 5, pp. 814-824, May 1990.

[27] J. A. Pereda, L. A. Vielva, A. Vegas, and A. Prieto, "Computation of resonant frequencies and quality factors of open dielectric resonators by a combination of the FDTD and Prony's methods," *IEEE Microwave Guided Wave Lett.*, vol. 2, no. 11, pp. 431-433, November 1992.

[28] K. Naishadham, "De-Embedding Intrinsic Parameters of High-Q Dielectric Resonators from Noisy Measurements," *Microwave and Optical Technology Letters*, vol. 48, no. 8, pp. 1453-1458, Aug. 2006.

[29] W. Ko and R. Mittra, "A combination of FD-TD and Prony's methods for analyzing microwave integrated circuits," *IEEE Trans. Microwave Theory Tech.*, vol. MTT-39, no. 12, pp. 2176-2181, December 1991.

[30] B. Houshmand, T.W. Huang, and T. Itoh, "Microwave structure characterization by a combination of FDTD and system identification methods," *IEEE Microwave and Guided Wave Lett.*, vol. 3, no. 8, pp. 262-264, August 1993.

[31] K. Naishadham and X. P. Lin, "Application of spectral domain Prony's method to the FDTD analysis of planar microstrip circuits," *IEEE Trans. Microwave Theory Tech.*, vol. MTT-42, no. 12, pp. 2391-2398, December 1994.

[32] R. S. Adve, T. K. Sarkar, O. M. C. Pereira-Filho, and S. M. Rao, "Extrapolation of time-domain responses from three-dimensional conducting objects utilizing the matrix pencil technique," *IEEE Trans. Antennas Propagat.*, vol. 45, no. 1, pp. 147-156, Jan. 1997.

[33] A. K. Shaw and K. Naishadham, "ARMA-based time-signature estimator for FDTD analysis of resonant structures," *IEEE Trans. Antennas Propagat.*, vol. AP-49, no. 3, pp. 327-339, March 2001.

[34] K. Naishadham and J. E. Piou, "Representation of Electromagnetic Responses in Time Domain Using State Space System Identification Method," *IEEE Trans. Antennas and Propagation*, vol. 64, no. 4, pp. 1404-1415, April 2016.

[35] Y. Wang and H. Ling, "Multimode parameter extraction for multiconductor transmission lines via single-pass FDTD and signal processing techniques," *IEEE Trans. Microwave Theory Tech.*, vol. MTT-46, no. 1, pp. 89-96, January 1998.

[36] K. Naishadham, J. Muldavin, and J. E. Piou, "Broadband Parametric Representation of Packaged MEMS Interconnects Using a Robust State Space Spectral Model," *Microwave and Optical Technology Letters*, vol. 50, no. 6, pp. 1482-1485, June 2008.

[37] M. McClure, R. C. Qiu, and L. Carin, "On the super-resolution identification of observables from swept-frequency data," *IEEE Trans. Antennas Propagat.*, vol. AP-45, no. 4, pp 631-641, April 1997.

[38] M. L. Burrows, "Two-dimensional ESPRIT with tracking for radar imaging and feature extraction," *IEEE Trans. Antennas Propagat.*, vol. AP-52, no. 2, pp. 524-532, February 2004.

[39] K. Naishadham and J. E. Piou, "State-Space Spectral Estimation of Characteristic Electromagnetic Responses in Wideband Data," *IEEE Antennas and Wireless Propagation Letters*, DOI: 10.1109/LAWP.2005.859386, October 2005.

[40] K. Naishadham and J. E. Piou, "A Robust State Space Model for the Characterization of Extended Returns in Radar Target Signatures," *IEEE Trans. Antennas and Propagation*, vol. 56, no. 6, pp. 1742-1751, June 2008.

[41] K. Naishadham, J. E. Piou, L. Ren, and A. E. Fathy, "Detection of Cardiopulmonary Parameters from Ultra-Wideband Radar Measurements Using the State Space Method," *IEEE Trans. Biomedical Circuits and Systems*, vol. 10, no. 6, pp. 1037-1046, Dec. 2016.

[42] L. Ren, H. Wang, K. Naishadham, O. Kilic, and A. E. Fathy, "Phase-Based Methods for Heart Rate Detection Using UWB Impulse Doppler Radar," *IEEE Trans. Microwave Theory Tech*., Vol. 64, No. 10, pp. 3319-3331, Oct. 2016.

[43] L. Ren, N. Tran, H. Wang, K. Naishadham, J. E. Piou, O. Kilic, and A. E. Fathy, "Short-Time State Space Method for Micro-Doppler Identification of Walking Subjects using UWB Impulse Doppler Radar," *IEEE Trans. Microwave Theory Tech*., vol. MTT-66, no. 7, pp. 3521-3534, May 2018.

[44] A. Sahin and E. L. Miller, "GPR localization of buried multiple objects using high resolution array processing," *Proc. Progress in Electromagnetics Research Symposium*, Cambridge, MA, July 1997.

[45] P. Stoica and A. Nehorai, "MUSIC, maximum likelihood and Cramer-Rao bound," *IEEE Trans. Acoust., Speech, Signal Processing*, vol. 37, pp. 720-741, May 1989.

[46] P. Stoica and A. Nehorai, "Performance comparison of subspace rotation and MUSIC methods for direction estimation," *IEEE Trans. Acoust., Speech, Signal Processing*, vol. 39, no. 2, pp. 446-453, Feb. 1991.

[47] B. D. Rao and K. V. S. Hari, "Performance analysis of TAM and ESPRIT for determining the direction of arrival of plane waves in noise," *IEEE Trans. Acoust., Speech, Signal Processing*, vol. 37. pp. 1990-1995, Dec. 1989.

[48] Y. Hua and T. K. Sarkar, "Matrix pencil method and its performance," in *Proc. IEEE ICASSP*, pp. 2476-2479, Apr. 1988.

[49] Y. Hua and T. K. Sarkar, "On SVD for estimating generalized eigenvalues of singular matrix pencil in noise," *IEEE Trans. Acoust., Speech, Signal Processing*, vol. ASSP-39, pp. 892-900, April 1991.

[50] B. D. Rao, "Sensitivity considerations in state space model-based harmonic retrieval methods," *IEEE Trans. Acoust., Speech, Signal Processing*, vol. 37, pp. 1789-1794. Nov. 1989.

[51] B. D. Rao, "Sensitivity analysis of state space methods in spectrum estimation," in *Proc. ICASSP*, Apr. 1987.

[52] J. E. Piou, K. M. Cuomo, and J. T. Mayhan, "A state space technique for ultrawide-bandwidth coherent processing," Massachusetts Institute of Technology, Lincoln Laboratory, Technical Report (TR) 1054, July 1999.

[53] J. E. Piou, "A state identification method for 1-D measurements with spectral gaps," *AIAA Guidance Navigation and Control Conference*, San Francisco, CA, August 2005, Paper No. 2005-5943.

[54] K. M. Cuomo, J. E. Piou, and J. T. Mayhan, "Ultrawideband coherent processing," *IEEE Trans. Antennas Propagat.*, vol. 47, no. 6, pp 1094-1107, June 1999.

[55] B. D. Rao, "Relationship between matrix pencil and state space based harmonic retrieval methods," *IEEE Trans. Acoust., Speech, Signal Processing*, vol. ASSP-38, pp. 177-179, Jan. 1990.

[56] S. Jang, W. Choi, T. K. Sarkar, and E. L. Mokole, "Quantitative comparison between matrix pencil method and state space-based methods for radar object identification," *Radio Science Bulletin*, no. 313, pp. 27-38, June 2005.

[57] M. Viberg, "Subspace-based methods for the identification of linear time-invariant systems," *Automatica*, vol. 31, pp. 1835-1851, 1995.

[58] P. V. Overschee and B. De Moor, Subspace Identification for Linear Systems: Theory, Implementation and Applications, Norwell, MA: Kluwer, 1996.

[59] C. T. Chou and J. M. Maciejowski, "System identification using balanced parametrizations," *IEEE Trans. Automat. Contr.*, vol. 42, pp. 956-974, July 1997.

[60] P. M. Makila, "State space identification of stable systems," *Int. J. Control*, vol. 72, pp. 193-205, 1999.

[61] J. E. Piou, K. M. Cuomo, and J. T. Mayhan, "Algorithm Development and Performance Bounds for Sparse-Band, Sparse-Angle Processing," Project Report NTP-4, MIT Lincoln Laboratory, Lexington, MA, June 2001.

[62] J. E. Piou, "Balanced realization for 2-D data fusion," *AIAA Guidance Navigation and Control Conference*, San Francisco, CA, August 2005, Paper No. 2005-5964.

[63] T. Kailath, *Linear Systems*, Prentice-Hall, Englewood Cliffs, N.J., 1980.

[64] K. Ogata, *Discrete-Time Control Systems*, New York: Prentice-Hall, 1987.

[65] R. E. Kalman, "Mathematical Description of Linear Dynamical Systems," *SIAM Journal Series A Control Theory*, vol. 1, no. 2, pp. 152-192, 1963.

[66] J. Rissanen, "Modeling by shortest data description," *Automatica*, vol. 14, no. 5, pp. 465-471, 1978.

[67] H. Akaike, "A new look at the statistical model identification," *IEEE Trans. Automat. Contr.*, vol. 19, pp. 716-723, June 1974.

[68] M. Wax and T. Kailath, "Detection of signals by information theoretic criteria," *IEEE Trans. Acoust., Speech, Signal Processing*, vol. 33, pp. 387-392, April 1985.

[69] M. Wax and I. Ziskind, "Detection of the number of coherent signals by the MDL principle," *IEEE Trans. Acoust., Speech, Signal Processing*, vol. 27, pp. 1190-1196, Aug. 1989.

[70] A. D. Droitcour, O. Boric-Lubecke and G. T. A. Kovacs, "Signal-to-noise ratio in Doppler radar system for heart and respiratory rate measurements," *IEEE Trans. Microwave Theory Tech.*, vol. 57, no. 10, pp. 2498-2507, October 2009.

[71] D. K. Cheng, *Field and Wave Electromagnetics*, Addison-Wesley, 1989, Chapter 9, p. 474.

[72] R. F. Harrington, *Time Harmonic Electromagnetic Fields*, McGraw-Hill, New York, 1961, Chapter 6.

[73] T. B. A. Senior and R. F. Goodrich, "Scattering by a sphere," *Proc. IEE (London)*, vol. 111, pp. 907-916, May 1964.

[74] L. B. Felsen and N. Marcuvitz, *Radiation and Scattering of Waves*, Prentice Hall, Englewood Cliffs, NJ, 1973, Chapter 6.

[75] K. Naishadham and J. E. Piou, "A novel one-dimensional block-processing approach to two-dimensional NMR spectroscopy," *IEEE International Symp. Biomedical Imaging*, Washington, DC, April 2007.

[76] J. E. Piou, K. Naishadham, and A. E. Fathy, "A one-dimensional block processing method for non-invasive detection of cardiac and respiratory rates," *IEEE Radar Conference*, Oklahoma City, OK, Apr. 2018.

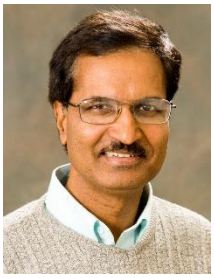

Krishna Naishadham received M.S. from Syracuse University and the Ph.D. from the University of Mississippi, both in Electrical Engineering, in 1982 and 1987, respectively. He served on the faculty of Electrical Engineering for 15 years at the University of Kentucky and Wright State University (tenured Professor). From 2002-2008, as a Research Scientist at MIT Lincoln Laboratory, he contributed innovative hybrid asymptotic techniques and spectral estimation methods for EM signature analysis and target feature extraction from radar data. In 2008, he joined Georgia Institute of Technology, where he is currently a Research Professor in the School of ECE. In 2013 he founded Wi-Sense, a startup research firm funded by the National Institutes of Health investigating cutting-edge wearable electronic and RF sensing devices for environmental, medical and health applications. His current research focuses on novel nanotechnology and semiconductor-based sensors for public health and the Internet of Things, as well as multifunctional antenna arrays and beamforming for 5G applications. Dr. Naishadham published four Book Chapters and over 180 papers in professional journals and conference proceedings. He was Chair of the Joint IEEE AP/MTT Chapter at Atlanta and served on the Technical Program Committee for the International Microwave Symposium (1993-2013). In the 2017-18 academic year he was a Visiting Professor in the Department of Electronics and Telecommunications at the Politecnico Di Torino in Torino, Italy. He also held Visiting Research Scientist positions at Ghent University, Ghent, Belgium (2013) and at Fudan University, Shanghai, China (2014).

Jean E Piou received M.S., Master of Philosophy (M.Ph.) and Ph.D. degrees in Electrical Engineering from the City University of New York (CUNY), USA, in 1987, 1990 and 1993, respectively. During his graduate study, his research areas included controller design for autopilots and eigenstructure assignment for aircrafts and space vehicles; he has authored several technical papers in those fields. Upon graduation, he held visiting professorship at the City University of New York, and assistant professorship at the State University of New York at Binghamton, USA. In 1995 Dr. Piou moved to Massachusetts, USA, where he is an independent research scientist. During his first fifteen years in Massachusetts, he worked on many projects where he developed advanced multi-dimensional signal processing techniques to characterize radar targets. For the past seven years, Dr. Piou conducted multi-disciplinary research involving automatic control theory, signal processing, spectral estimation and imaging techniques. He has published many technical reports, journal articles and conference papers in the fields of automatic control signal processing, spectral estimation, sensor fusion and imaging. Dr. Piou is a senior member of the American Institute of Aeronautics and Astronautics (AIAA) since 1998.